Electronic Supplementary Material (ESI) for Physical Chemistry Chemical Physics.

Supplementary Information:

Satellite ligand effects on magnetic exchange in dimers. A structural, magnetic and theoretical investigation of $Cu_2L_2X_4$ (L = methylisothiazolinone and X = Cl^-, Br^-)

Stefan Coetzee,[a] Mark M. Turnbull,[b] Christopher P. Landee,[c] Jeffrey C. Monroe,[c] Mercè Deumal,[d] Juan J. Novoa,[e] Melanie Rademeyer[a]*

[a] Department of Chemistry, University of Pretoria, Pretoria, 0002, South Africa

[b] Carlson School of Chemistry and Biochemistry, Clark University, 950 Main St., Worcester, Massachusetts, 01610, USA

[c] Department of Physics, Clark University, 950 Main St., Worcester, Massachusetts, 01610, USA

[d] Serra-Húnter Fellow, Departament de Ciència de Materials i Química Física and IQTCUB, Facultat de Química, Universitat de Barcelona, Martí i Franquès 1, 08028, Barcelona, Spain

[e] Departament de Ciència de Materials i Química Física and IQTCUB, Facultat de Química, Universitat de Barcelona, Martí i Franquès 1, 08028, Barcelona, Spain

E-mail: melanie.rademeyer@up.ac.za

Section 1 – Crystallographic data and Powder X-ray Diffraction (PXRD) Patterns

The new structure of **CuBrMI** was determined in this study. Table S1.1 displays the crystallographic parameters of the **CuBrMI** and **CuClMI** structures, and Table S1.2 for selected bond lengths and angles). Experimental PXRD patterns of the bulk samples were compared with powder patterns calculated from the single crystal structures, in order to determine if the single crystal is representative of the bulk sample. Note that the comparison confirms the phase purity of the powder samples. The software DiffractWD[1] was employed for this comparison. The experimental powder patterns are shown in red and the calculated patterns are given in black for **CuClMI** and **CuBrMI** in Fig. S1.1 and Fig. S1.2, respectively.

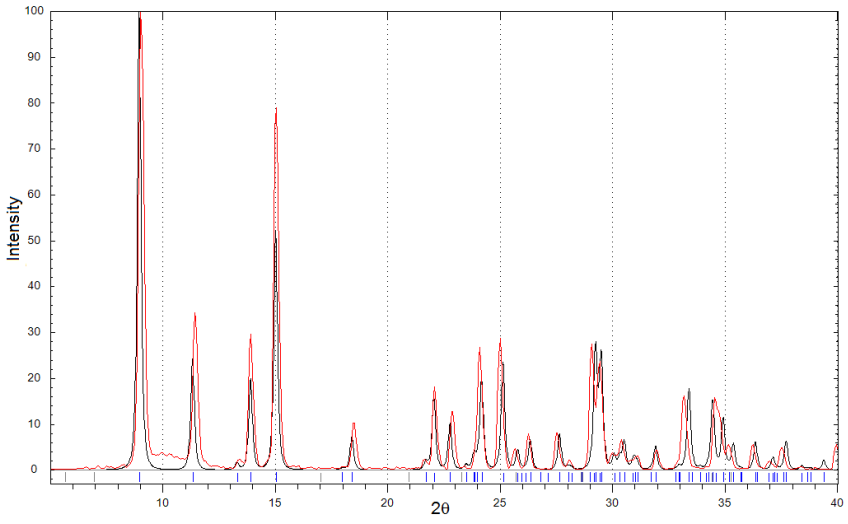

Figure S1.1. Calculated **CuClMI** powder X-ray diffraction (black) *vs.* experimental pattern (red).

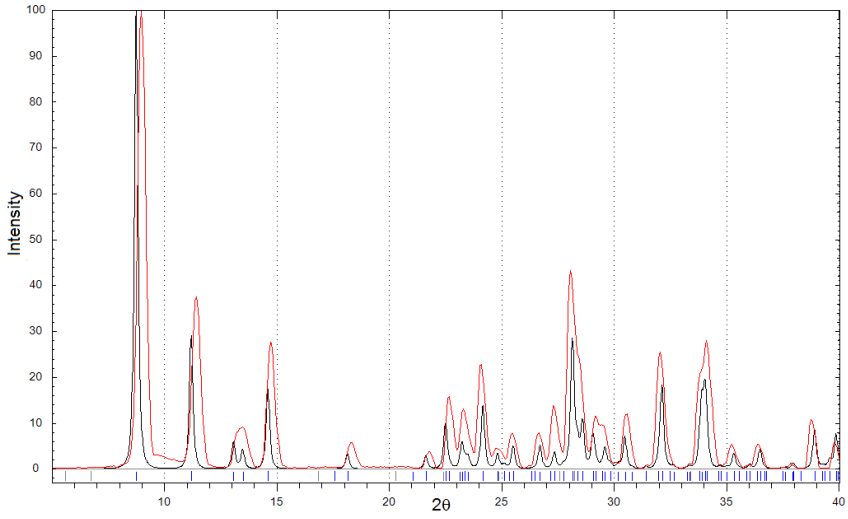

Figure S1.2. Calculated **CuBrMI** powder X-ray diffraction (black) *vs.* experimental pattern (red).

Table S1.1. Crystallographic parameters of **CuBrMI**. The crystallographic data of **CuClMI**[2] are included for comparison purposes.

Abbreviation	CuClMI[2]	CuBrMI
Name	bis(μ2-chloro)-dichloro-bis(2-methyl-1,2-thiazol-3(2H)-one)-di-copper(II)	bis(μ2-bromo)-dicbromo-bis(2-methyl-1,2-thiazol-3(2H)-one)-di-copper(II)
Empirical formula	$[CuCl_2(C_4H_5NOS)]_\infty$	$[CuBr_2(C_4H_5NOS)]_\infty$
Formula weight (g.mol^{-1})	249.60	338.51
Temperature (K)	173	150
Wavelength (Å)	-	0.71073
Crystal system	Monoclinic	Monoclinic
Space group	$P2_1/n$	$P2_1/n$
***a* (Å)**	3.8434(8)	3.9875(2)
***b* (Å)**	15.597(4)	15.7850(10)
***c* (Å)**	12.810(3)	13.2012(9)
α (°)	90	90
β (°)	96.930(7)	96.532(2)
γ (°)	90	90
Volume (Å^3)	762.292	825.525
Z	4	4
Density calculated (g.cm^{-3})	2.175	2.724
Absorption coefficient (mm^{-1})	-	12.508
***F*(000)**	-	636
Crystal size (mm^3)	-	0.073 x 0.106 x 0.150
Reflections collected	-	20574
Unique Reflections	-	1682
Completeness	-	99.8 %
Parameters	-	111
Goodness-of-fit F^2	-	1.177
Final R indices [I>2σ(I)]	-	0.0237
R indices (all data)	-	0.0264

Table S1.2. Selected bond lengths and angles in **CuClMI**[2] and **CuBrMI**.

	CuClMI[2] X = Cl$^-$	**CuBrMI X = Br$^-$**	**Description**
Cu1–O1 (Å)	1.940(3)	1.931(3)	
Cu1–X1 (Å)	2.261(2)	2.4074(6)	Dimer terminal
Cu1–X2$^{\#1}$ (Å)	2.322(2)	2.4574(5)	Dimer bridging
Cu1–X2 (Å)	2.282(2)	2.4132(6)	Dimer bridging
Cu1···X1 (Å)	2.885(1)	3.0220(5)	Inter-dimer (terminal semi-coordinate)
Cu1···X2 (Å)	3.041(1)	3.1967(5)	Inter-dimer (bridging semi-coordinate)
X1–Cu1–X2 (°)	93.28(5)	93.23(2)	Dimer
X1–Cu1–X2$^{\#1}$ (°)	175.61(6)	175.70(2)	Dimer
X2–Cu1–X2$^{\#1}$ (°)	84.59(5)	85.37(2)	Dimer
Cu1–X2–Cu1$^{\#1}$ (°)	95.41(5)	94.63(2)	Dimer
Cu1–X1–Cu1 (°)	95.87(5)	93.83(2)	Inter-dimer (terminal semi-coordinate)
Cu1–X2–Cu1 (°)	90.53(4)	88.66(1)	Inter-dimer (bridging semi-coordinate)
X1–Cu–X2 (°)	93.18(5)	92.89(2)	Inter-dimer (semi-coordinate)

Symmetry operator: #1: -x+2,-y+1,-z+1

Section 2 - Dimer and Tetramer Cluster Models

In this section, the First-Principles, Bottom-Up (FPBU) method[3] is discussed as it was applied to **CuClMI** and **CuBrMI**. The J_{AB} magnetic exchange coupling between A and B spin-carrying units was evaluated using two different cluster models, namely a simple dimer and more extended tetramer models, by means of Gaussian[4] and Orca[5], respectively. Irrespective of the model, a given J_{AB} interaction is calculated as the energy difference between high-spin and low-spin states. Note here that, since all energies are evaluated at UDFT/UB3LYP level, we use the broken-symmetry approach to obtain open-shell low-spin solutions (e.g. singlet and triplet when using a tetramer model, and singlet when the model is a dimer). High-spin states (triplet for dimer model and sextet for tetramer model) have basically no spin contamination, namely, $<S^2>$ is 2.01 for triplet and 6.01 for sextet states. Typical values of spin contamination were encountered for low-spin states, such as singlet using dimer models and triplet/singlet states using tetramer models (specifically, $<S^2>$ is 0.999 for singlet BS solution, which after spin annihilation becomes 0.040 using Gaussian, and 3.01 for triplet and 2.00 for singlet using Orca, which are then corrected via spin projection). The results obtained for J_{AB} using both dimer and tetramer models are next discussed in this section.

For **CuXMI**, nine potential pairs of radicals (d_1-d_9) were identified from the crystal structures of **CuClMI**[2] and **CuBrMI** up to a cut-off distance of ~10 Å between Cu(II) ions (see Fig. S2.1). This distance corresponds to the maximum distance between two neighboring polymeric chains.

d_1 is the radical pair comprised of the Cu(II) ions in the $Cu_2(MI)_2X_4$ dimeric unit (in red in Fig. S2.1(a,e)). The radical pair in d_2 contains fragments of two neighboring stacked dimers along the polymer axis (in blue in Fig. S2.1(b,e)). d_3 contains the Cu(II) ions from two neighboring dimeric units diagonally across the dimeric unit shown in Fig. S2.1(c,e), and d_4 is similarly a diagonal interaction shown in Fig. S2.1(d,e). d_1-d_4 are potential interactions within the 1D polymers whereas d_5-d_9 are interactions between the polymers, shown in Fig. S2.1(f). Due to the $P2_1/n$ symmetry of both compounds, d_5-d_9 are propagated by symmetry along the *b*- and *c*-axes. The potential magnetic topology of

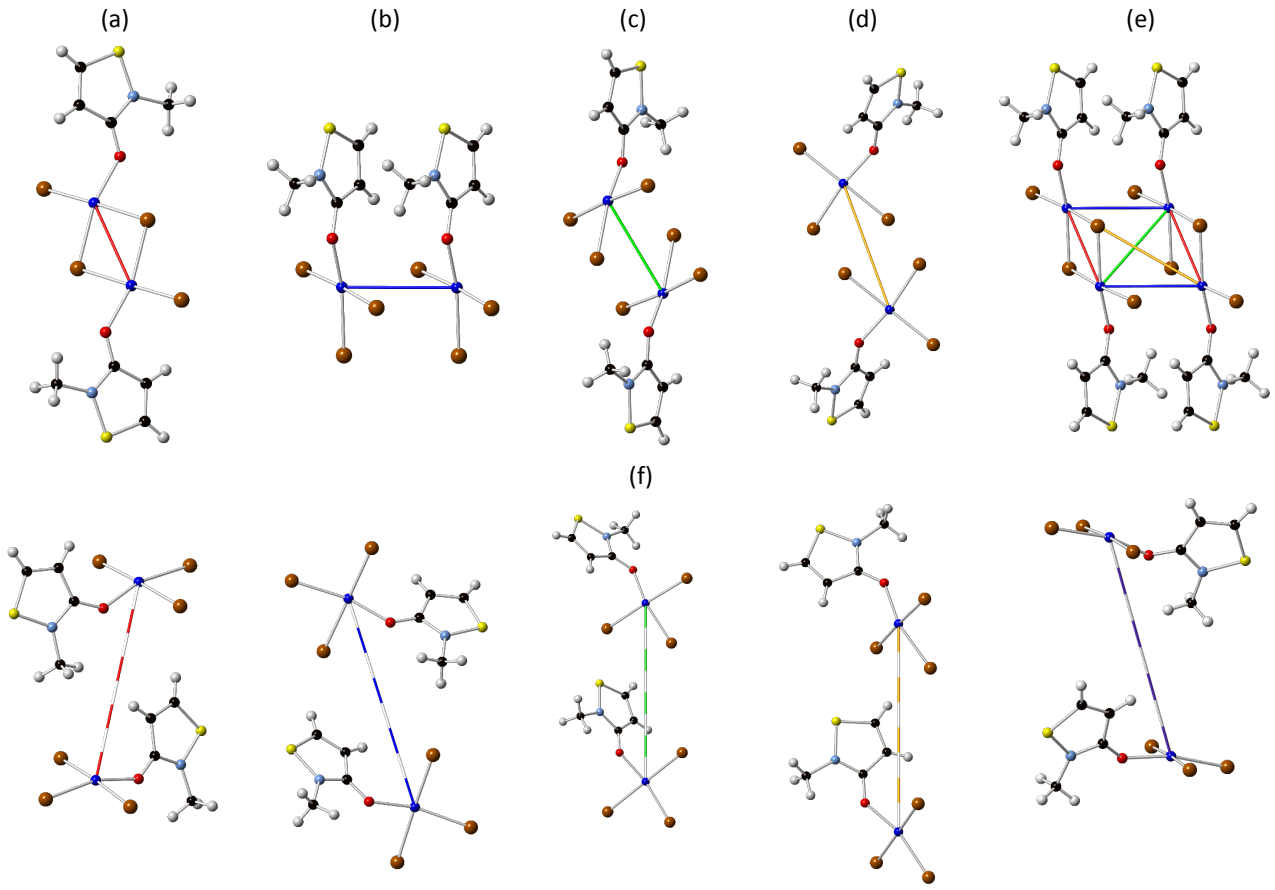

Figure S2.1. Dimer finite cluster models for **CuBrMI** for (a) d_1, (b) d_2 ,(c) d_3, (d) d_4 and (f) d_5-d_9. (e) Tetrameric finite cluster model for **CuBrMI** showing interactions d_1 to d_4. Atom colors: Cu (blue), Cl (green), Br (brown), C (black), O (red), N (light blue), S (yellow) and H (white). Coloured lines indicate the exchange interactions: J_1 (red), J_2 (blue), J_3 (green), and J_4 (orange), J_5 (red dashed), J_6 (blue dashed), J_7 (green dashed), J_8 (orange dashed), J_9 (purple dashed). d_i distances are given in Table 4 in the main text.

both **CuClMI** and **CuBrMI** can be described as 1D magnetic chains along the *a*-axis, with potential next-nearest-neighbor (NNN) interactions along the chain as well as symmetry-related interactions along the other two directions to form potential 3D magnetic networks.

Finite clusters for both compounds were constructed from the crystal structures in such a way that the chemical environments around these clusters are chemically representative of the environment around the Cu(II) ions. Square planar arrangements and tetrameric units of halides and MI ligands coordinated to the Cu(II) ions were considered and modelled as shown in Fig. S2.1, i.e. using both dimer and tetramer models. J_i indicates the magnetic exchange interaction in radical pair d_i.

Table S2.1. Computed DFT J_i values for **CuClMI** and **CuBrMI**. Note that d_i stands for the Cu···Cu distance

	CuClMI			CuBrMI		
i	**d_i (Å)**	**J_{iD} (cm^{-1})**	**J_{iT} (cm^{-1})**	**d_i (Å)**	**J_{iD} (cm^{-1})**	**J_{iT} (cm^{-1})**
		Dimer	**Tetramer**		**Dimer**	**Tetramer**
1	3.406	28.16 †	33.51	3.5805	42.10	49.16
2	3.843	0.61	0.12	3.9875	1.15	0.03
3	3.949	-5.55	-2.83	4.1328	-9.81	-6.09
4	6.095	1.12	-0.10	6.3530	2.26	0.09
5	8.38	0		8.5348	0.01	
6	8.727	0.03		8.8787	0.05	
7	9.081	0.02		9.1958	0.08	
8	9.343	0		9.4981	0	
9	9.6864	0		9.9325	0	

For J_{iD} and J_{iT}, the "D" and "T" refer to the dimer and tetramer models.
†Compared to Ref. 2: J_1 calc. = +28.16 cm^{-1}, J_1 fit = +5.03 cm^{-1}.

Table S2.1 lists the calculated magnetic exchange interactions for the different radical pairs, with J_{iD} referring to the value obtained using a dimer model, and J_{iT} indicating the exchange interaction obtained using a tetramer model.

The value of J_{1D} for **CuClMI** is essentially identical to the one calculated originally.[2] The J_{iD} values are slightly different, compared to the J_{iT} values for each compound, with larger differences evident for $J_2 - J_4$. It is, however, expected that the tetramer model will outperform the dimer model, as the chemical environment around the Cu(II) ions will be represented better in the tetramer models.

Due to the larger size of the Br^- ligand compared to the Cl^- ligand, the different amount of orbital overlap, S_{ab}, that the different pairs of **CuXMI** radicals exhibit (e.g. $S_{ab}(d_1) >> S_{ab}(d_{i\neq1})$) will, in turn, affect the numerical value of the radical···radical coupling (see Eq. 1 in the main text) and thus modulate the value of J_i magnetic coupling ($J_{i,\,Br} > J_{i,\,Cl}$).

The closer spacing of polymer chains in the structure of **CuBrMI** and the bromide's more diffuse orbitals translate into a very small amount of magnetic exchange between polymer chains in **CuBrMI** compared to the insignificant exchange observed for **CuClMI**. In **CuBrMI**, the J_5, J_8, and J_9 interactions are insignificant. As for the J_6 interaction, it is a very weak FM interaction due to a Cu-X···X-Cu interaction with X···X distance of 6.06 Å.

The J_7 interaction is also a very weak FM interaction, and involves two possible Cu-X···X-Cu double halide exchange pathways: (i) a Cu-X_{trans}···X_{cis}-Cu interaction with X···X distance of 6.06 Å, and (ii) a Cu-X_{cis}···X_{cis}-Cu with X···X distance of 8.16 Å. It is important to note that these interactions are very small and their impact on the bulk properties is negligible.

The tetramer models were shown to reproduce the bulk magnetic properties better than the dimer models. The dimer cluster models estimate J_1 relatively well, with an absolute "error" of ~5 cm^{-1} which is within 15%. The estimation of the smaller exchange interactions are in the same order of absolute error, but in relative terms, the dimer model overestimates J_2, J_3, and even calculates an AFM value for J_4.

Section 3 - Discussion Of Magnetic Models And Their Calculated Magnetic Susceptibility

The choice of the most adequate magnetic model is key to reproduce the experimental data. Therefore, we will here give more details on how to address it. Let us then start by reminding that based on the value of the significant J_{AB} interactions, a magnetic topology is constructed. According to the effective Hamiltonian theory,[6,7] a finite effective Hamiltonian can be constructed such that, when it is applied to an appropriate model space that is representative of the bulk of the material, it yields a set of energy eigenvalues that match those of the exact Hamiltonian when diagonalised fully. A good magnetic model should include the most relevant J_{AB} interactions, and have topological connectivity similar to the bulk of the material. Computationally, the number of radicals for this approach is limited to 18, but generally, 16 radicals are preferred for computational efficiency. In summary, the magnetic model is extracted from the magnetic topology and consists of an even number of radicals. Note that the sum on the Hamiltonian $\widehat{H} = -2\sum_{A<B} J_{AB}\,\hat{\hat{S}}_A \cdot \hat{\hat{S}}_B$ runs for all unique combinations of two different A and B radicals forming the magnetic model. From this diagonalization, the E_n energy eigenvalue and the S_n total spin number of each respective *n* state are determined. No interactions are excluded *a priori*, and multiple arrangements and connectivities are tested to obtain a model that best mimics the experimental data. Note that a good model should display a convergence toward the experimental values as the number of radicals is increased in the effective Hamiltonian. In this case, the magnetic property of interest is the magnetic susceptibility, which is calculated using the usual statistical mechanics expression.[8]

$$\chi = \frac{N_A g^2 \mu_B^2}{3 k_B T \mu_0}\left[\frac{\sum_n S_n(S_n+1)(2S_n+1)exp\left[-\frac{E_n - E_0}{k_B T}\right]}{\sum_n (2S_n+1)exp\left[-\frac{E_n - E_0}{k_B T}\right]}\right]$$

where *g* is the gyromagnetic factor, and the constants N_A , μ_B , k_B and μ_0 are Avogadro's number, the Bohr magneton, the Boltzmann's constant, and the permeability of free space, respectively. S_n is the spin of the n-th energy level and E_n the microscopic energy levels obtained from the full diagonalisation of the Heisenberg Hamiltonian.

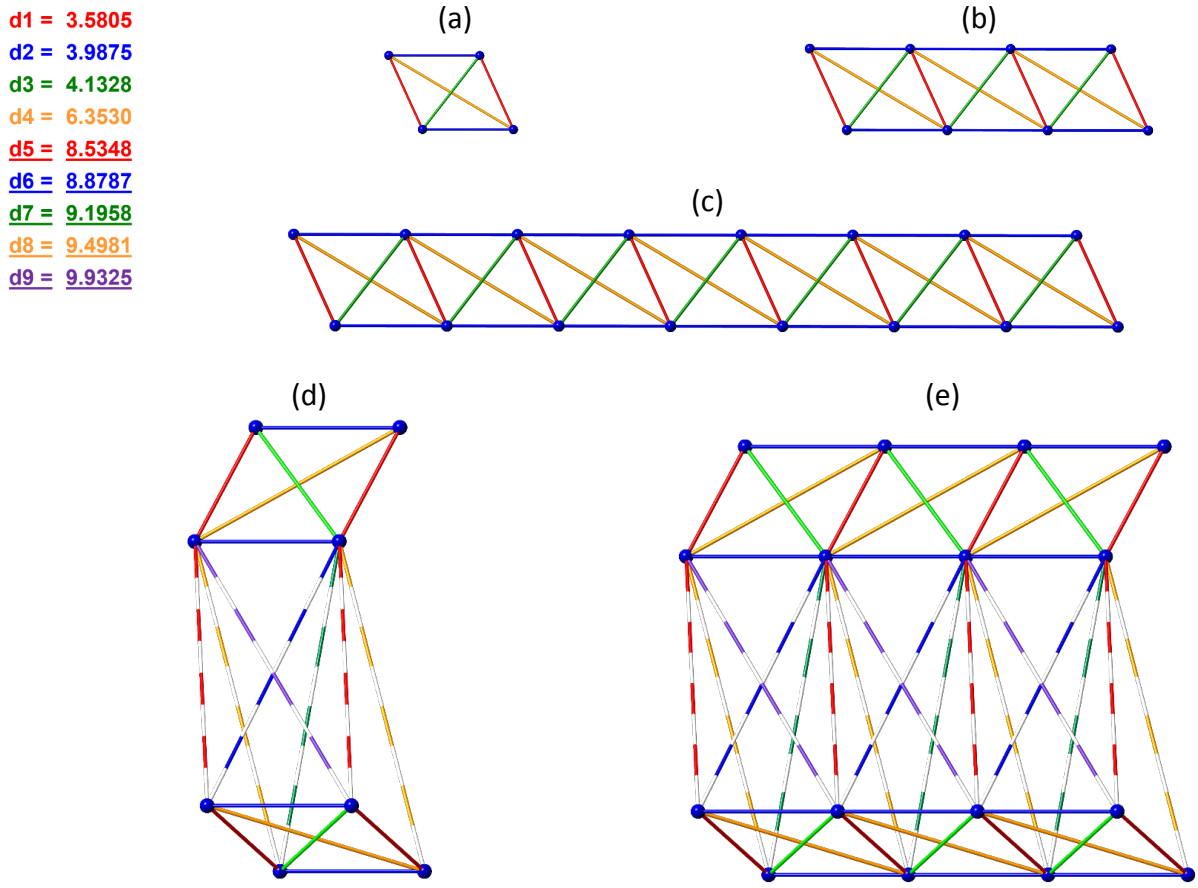

Figure S3.1. Magnetic models that were used to compute the susceptibility curves of **CuClMI (**and are representative of **CuBrMI**, with different distances). Intra-chain (a) 2x2 model, (b) 2x4 model, and (c) 2x8 model. Inter-chain interactions (IC) are evaluated along either (d) IC 2x2x2 or (e) IC 2x2x4. Distances are given in units of Å.

The magnetic models used to calculate the magnetic susceptibility data include cyclic and open models. Open models were used to explore the cooperativity between magnetic couplings along the *a*-, *b*-, and *c*-crystallographic axes, respectively. Models using the *J* values obtained from the dimer calculations (J_{iD}), as well as from the finite tetramer cluster models (J_{iT}), were considered for both compounds.

Firstly, the simplest chain magnetic model was enlarged from a 2x2 model (4 radicals) with two interacting dimers, to a 2x8 model (16 radicals) with eight dimers, along the *a*-axis (see Fig. S3.1(a)-(c) for models). For **CuXMI**, convergence toward the experimental curve is observed as the size of the models is increased. Convergence to experimental data is achieved with all the 2x8 models using J_{iT} (Fig. S3.2(a) and (b)) or J_{iD} (Fig. S3.2(c) and (d)) values for both compounds. For **CuBrMI** the open 2x8 model using J_{iD} replicates

the data more accurately, which is unexpected since a tetramer magnetic model replicates the environment of the magnetic interactions to be calculated better, and thus would be the model envisaged to perform better. This result is, however, flawed by the use of open chain models, as we will show next.

To test for the significance of interactions between chains (IC) in **CuBrMI** (**CuClMI** has no interchain interactions), two chains of 2x2 units (IC 2x2x2 model), and two chains of 2x4 units (IC 2x2x4 model), were also considered (see Fig. S3.1(d-e) for models). These are symmetry-related interactions and are therefore the same in the *b*- and *c*-directions. The $\chi_m(T)$ data overlaps with the calculated data for the corresponding 2x2 and 2x4 models (Fig. S3.3), indicating that the very weak FM interactions between the chains have no appreciable effect on the bulk χ_m data.

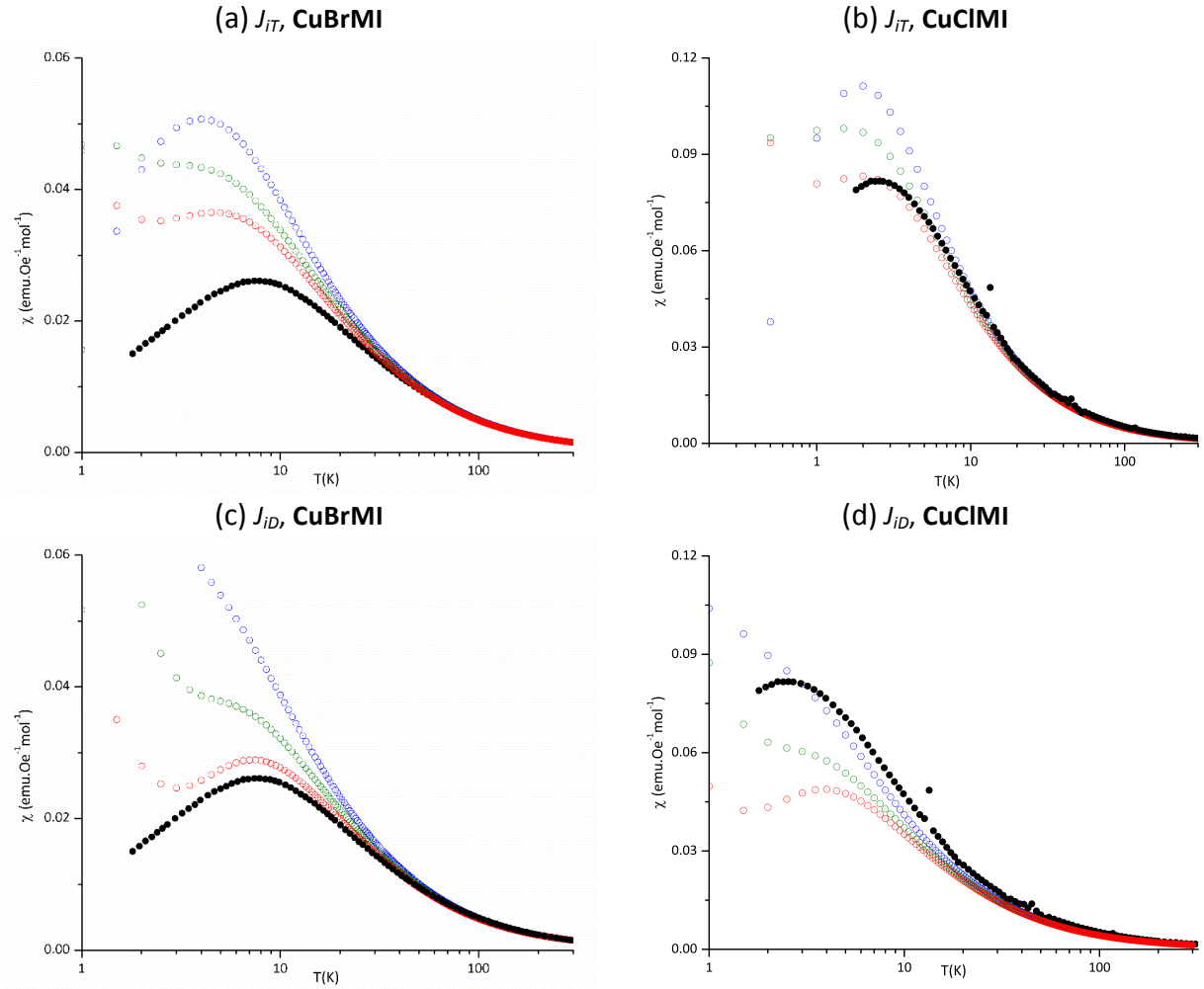

Figure S3.2. Magnetic susceptibility for (a) **CuBrMI** and (b) **CuClMI** using open chain magnetic models (J_{iT}) and using open chain (J_{iD}) models for (c) **CuBrMI** and (d) **CuClMI** : 2x2 model (blue), 2x4 model (green), and 2x8 model (red). Experimental data are also given (black).

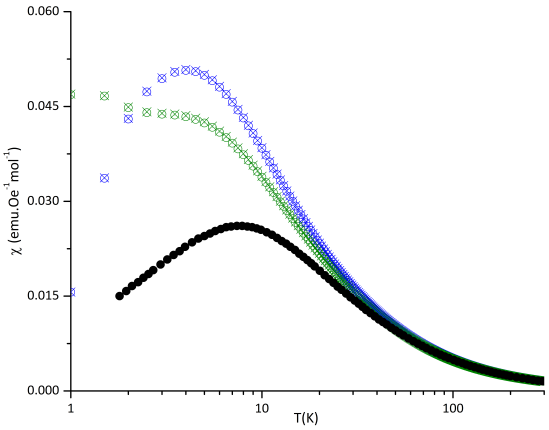

Figure S3.3. Magnetic susceptibility for **CuBrMI** using open chain magnetic models and corresponding inter-chain models: 2x2 model (blue circles), IC2x2x2 (blue cross), 2x4 model (green circles), and IC2x2x4 (green cross). Experimental data are also given (black).

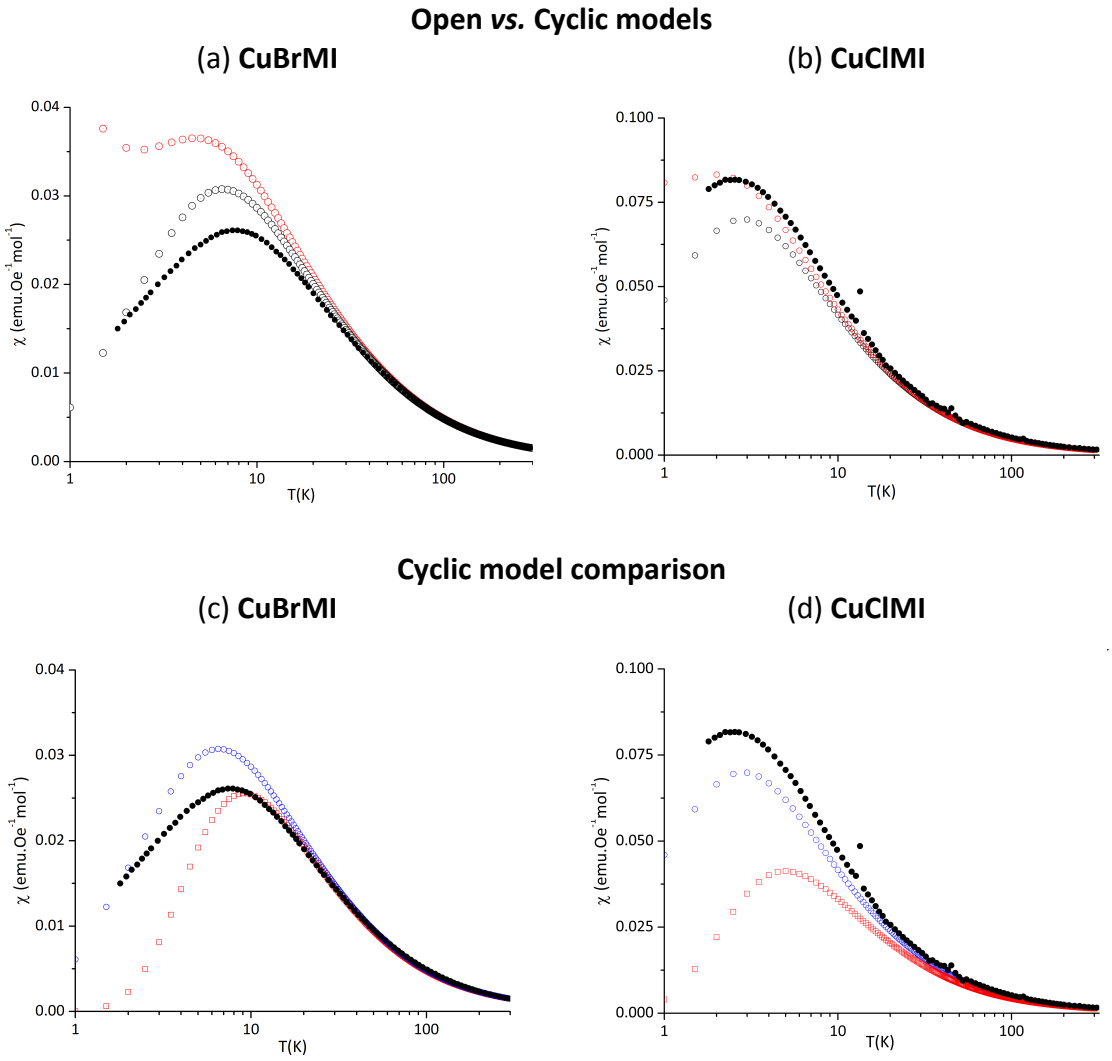

Figure S3.4. Magnetic susceptibility for (a) **CuBrMI** using open (red circles) and cyclic (black circles) 2x8 models, and (b) **CuClMI** using open (red circles) and cyclic (black circles) 2x8 models with J_{iT}. Experimental data is also given (black dots). Low temperature simulated $\chi_m(T)$ data for (c) **CuBrMI** and (d) **CuClMI**. Experimental (•), 2x8 cyclic model using J_{iD} (red squares) and 2x8 cyclic model using J_{iT} (blue circles).

In addition to the open models, cyclic versions of the 2x8 models were also considered. A comparison of the open and closed 2x8 models for both compounds shows that the 2x8 open models exhibit a FM tail, incorrectly indicating a FM ground state, while the cyclic model correctly predicts the singlet ground state, and accurately replicates the peak maxima and peak positions for both compounds, as shown in Fig. S3.4.

For **CuBrMI**, as the size of the model increases, the calculated susceptibility converges toward the experimental data. The best performing model overall is the 2x8 cyclic model which predicts the maximum in susceptibility of 0.031 emu.Oe^{-1}.mol^{-1} at 6.5 K (Exp: 0.026 emu.Oe^{-1}.mol^{-1} at 7.5 K) and correctly predicts an AFM ground state for **CuBrMI** as shown in Fig. S3.4(a). Note that magnetic susceptibility data calculated using J_{iT}'s resemble the experimental data more closely (see Fig. S3.4(c)). The addition of inter-chain interactions has no significant effect on the calculated susceptibility of both compounds. Regarding the experimental magnetic data recorded in this study for **CuClMI**, it is best replicated by the 2x8 cyclic model which predicts a maximum in the susceptibility of 0.070 emu.Oe^{-1}.mol^{-1} at 3 K (Exp: 0.082 emu.Oe^{-1}.mol^{-1} at 2.69 K) and correctly predicts an AFM ground state for **CuClMI** as shown in Fig. S3.4(b), in contrast with previously reported experimental observations.[2] Finally it should be noted that, although the 2x8 cyclic model using J_{iD} produced a good replication of the magnetic data for **CuClMI**, the position of the maximum in the peak susceptibility is reproduced better by the 2x8 cyclic model using J_{iT}, shown in Fig. S3.4 (c)-(d). Therefore, all discussion in main text will be based on J_{iT} calculated and simulated data.

Section 4 - Decomposition of J_{AB}

J_{AB} can be decomposed into direct exchange (J_0), kinetic exchange (ΔJ_{KE}), core-electrons polarisation (ΔJ_{CP}), and other sources (J_{Oth}) contributions:

$$J_{AB} = J_0 + \Delta J_{KE} + \Delta J_{CP} + J_{Oth}$$

J_0 is the direct exchange contribution that describes the extent to which magnetic molecular orbitals both have significant amplitudes in some space, despite being orthogonal.[9] This contribution is always FM and depends on the amount of electron density in the magnetic molecular orbitals.[10]

Anti-parallel electrons gain energy through delocalisation. The two extremes of this are (i) when an electron on site *a* delocalises completely on *b* to form an ionic valence bond (VB) $|a^+b^-|$, and (ii) the neutral VB form $|ab|$, which is more commonly known as the Anderson or superexchange mechanism.[11] ΔJ_{KE} provides a measure of the interaction of these two VB states. This contribution is always AFM because of the delocalisation of the unpaired electrons between magnetic molecular orbitals. ΔJ_{KE} is dependent on the Hopping integral *t*, and provides a measure of the probability of an electron jumping from one magnetic site to another, *via* ligand orbitals. In competition to the delocalisation of spins is an on-site repulsion of electrons, *U*, which is defined as the difference in energy between the two VB states.

ΔJ_{CP} is due to the creation of an exchange field by the magnetic orbitals. The interaction of the core-electrons with this field is the origin of this contribution to the magnetic exchange interaction.[12] This value provides a measure of the separation of α and β spin densities, thereby spin polarising the magnetic molecular orbitals.

Finally, J_{Oth} is the contribution of other effects that are not explicitly decomposed by this strategy.

This decomposition scheme[10] is based on broken-symmetry Kohn-Sham Density Functional Theory (BS-KSDFT) calculations using restricted open-shell (RO) methods following a 5-step procedure. (1) The magnetic orbitals are calculated with a localised RO

high spin M_S = 1 state (T,RO) without optimising any orbitals. (2) The spin is flipped in one of the magnetic orbitals to produce the broken-symmetry M_S = 0 solution (BS,RO). From this, J_0 is calculated as the difference in energy of the (BS,RO) and (T,RO) states. (3) The magnetic orbitals of the M_S = 0 states are then relaxed in a field of frozen non-magnetic orbitals allowing the full delocalisation of the magnetic orbitals (BS,UFC) to obtain the value of ΔJ_{KE}. (4) The core orbitals in both the M_S = 0 and M_S = 1 states (T,UFM) and (BS,UFM) are relaxed to determine the extent to which the core-electrons are polarised by the magnetic orbitals, ΔJ_{CP}. (5) The total magnetic interaction and the contribution to J from other sources are obtained by fully relaxing all orbitals in the broken-symmetry M_S = 0 and triplet M_S = 1 states, J_{AB} and J_{Oth}.

These calculations have to be performed on the tetramer clusters of **CuClMI**, **CuClMI(Rot)**, **CuBrMI**, **CuClPYR**, **CuBrBA**, **CuClBA**, and **$Cu_2Cl_6^{2-}$** . These tetramer models are a modelling challenge since the "*DecompositionPath*" method is limited to two spins. Therefore, the tetramer clusters were modified to only include two Cu(II) ions at a time, with the other Cu(II) ions substituted with diamagnetic Zn(II) ions, such to decompose J_1 and J_3 (see Fig. S4.1 for example using tetramer model of **CuClMI**).

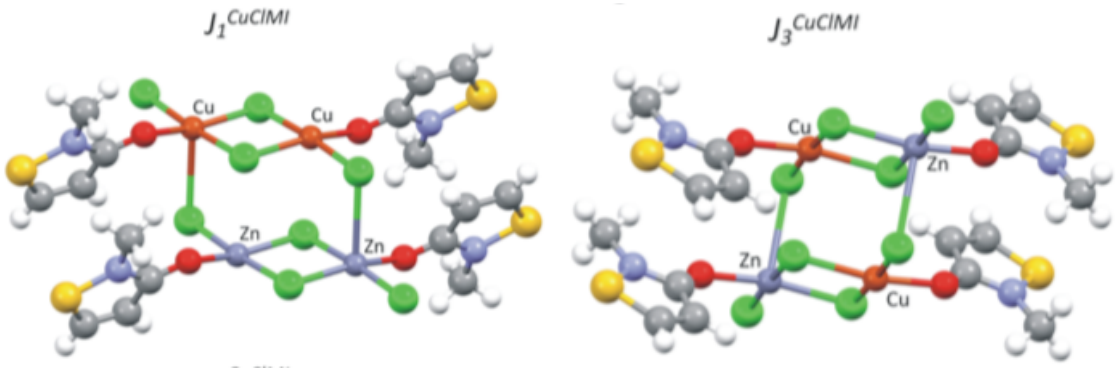

Figure S4.1. Structures used to decompose J_1 and J_3 via the J-decomposition scheme illustrated using the tetramer model of CuClMI.

Table S4.1. Values of J_i exchange interactions (in cm^{-1}) calculated using tetramer models with four Cu-moieties and those with two Cu(II) and two Zn(II) moieties.

compound	$J_{1T,\ 4\ Cu\text{-}moieties}$	$J_{1T,\ 2\ Cu\ +\ 2\ Zn\ moieties}$
CuClMI	33.5	32.9
	$J_{3T,\ 4\ Cu\text{-}moieties}$	$J_{3T,\ 2\ Cu\ +\ 2\ Zn\ moieties}$
CuClPYR	0.52	2.0
CuClBA	-6.2	-6.0

The values of J_1 and J_3 are calculated as a part of the decomposition procedure and listed in Table S4.1 for **CuClMI** and **CuClPYR**, **CuClBA**, respectively, to show three different sets of calculations. It is evident from the J_i values in Table S4.1 that the use of Zn(II) as a replacement diamagnetic ion for Cu(II) ions produces values for J_1 and J_3 that are similar to those of the tetrameric model for which the results are listed in Table 4 in main text (and Table S2.2 in SI Section 2 for CuClMI). This illustrates that Zn(II) is a viable diamagnetic replacement for Cu(II) when magnetic interaction calculations are limited to two spins. It thus follows that the results reported in the main text on the decomposition of J_{AB} for **CuClMI**, **CuClPYR** and **CuClBA** using a tetramer model will be obtained using models according to Fig. S4.1.

Section 5 - Analysis of CuClPYR

The results of the analysis of **CuClPYR** are given in this section. For a detailed discussion of the structures, the reader is referred to the original papers.[13] Note that the R-factor of the structure of **CuClPYR** was reported to be high, at 23.9 %, which may impact the quality of the theoretical calculations.

In **CuClPYR**, any two $Cu_2Cl_4(PYR)_2$ dimer units arrange such that there are two hydrogen bonds between them, namely, $(PYR\_dimer_1)O\cdots H\text{-}N(PYR\_dimer_2)$ at 2.111Å (see Fig. S5.1). Therefore, the calculations to evaluate the magnetic coupling between spin-carrying units will have to take into account the effect that hydrogen interactions might have on the value of J_{AB} coupling (see Fig. S5.2 for tetramer models and Table S5.1 for values).

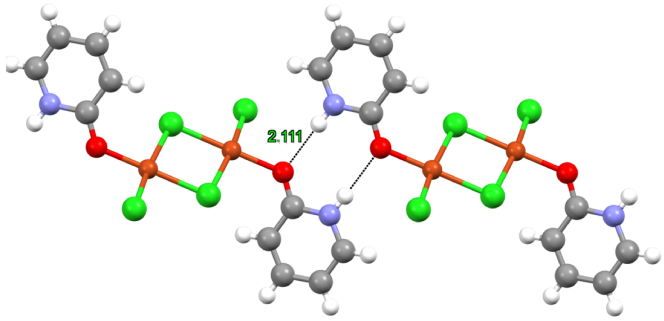

Figure S5.1. Dimer units of **CuClPYR**. Atoms were drawn with ball-and-stick models. Note that hydrogen bonds between $Cu_2Cl_4(PYR)_2$ units are highlighted (N-H···O distance is 2.111 Å). Atomic colours: C (grey), Cl (green), Cu (brown), H (white), N (blue), O (red).

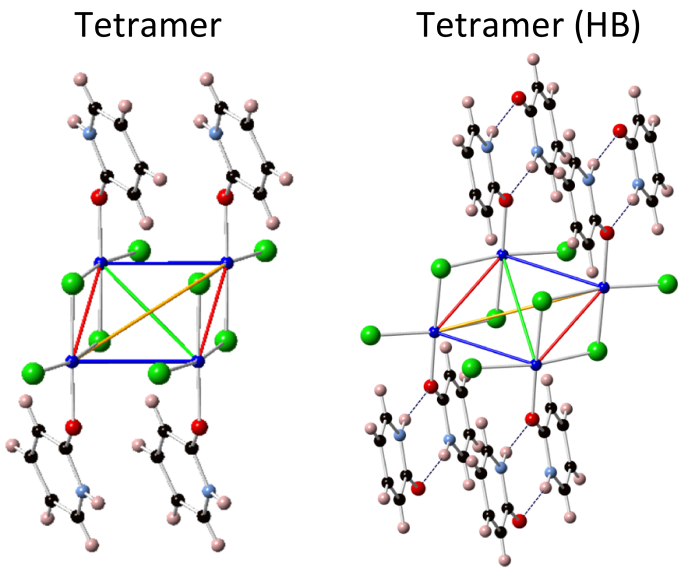

Figure S5.2. Tetramer and tetramer (HB) (with additional hydrogen bonded molecules) cluster models used to calculate J_i for **CuClPYR**. Note J_1 (red), J_2 (blue), J_3 (green), and J_4 (orange) are indicated.

Table S5.1 Computed DFT J_i values for **CuClPYR** using tetrameric models. HB and Non-HB refer to the tetramer finite cluster structures that either include or not additional PYR molecules that are hydrogen-bonded to the coordinating PYR molecules, as shown in Fig. S5.2.

d_i (Å)	**CuClPYR$_{Non-HB}$ J_i (cm^{-1}) Tetramer**	**CuClPYR$_{HB}$ J_i (cm^{-1}) Tetramer**
3.44(2)	11.67	19.26
3.84(4)	1.11	0.82
4.11(4)	0.36	0.52
6.02(5)	0.10	0.09
7.10(2)	-0.07*	-
7.46(4)	0.05*	-

* These values were calculated with dimer clusters of d_5 and d_6 .

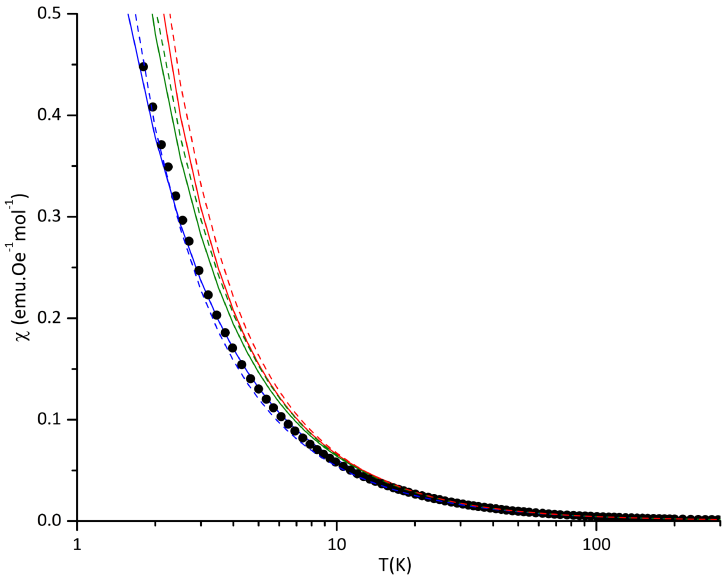

Figure S5.3. Simulated χ vs. T data for **CuClPYR**. Tetramer model results are shown as striped lines, while the hydrogen-bonded the 2x8 model including hydrogen-bonded molecules are shown as solid lines. Experimental (•), 2x2 model (o), 2x4 model (o), 2x8 model (o). Note the logarithmic temperature scale.

For **CuClPYR**, the tetramer (striped lines in Fig**.** S5.3) and hydrogen-bonded (solid lines in Fig. S5.3) tetramer models all replicate the magnetic data excellently with small differences amplified by the logarithmic scales used in Fig. S5.3. As the size of the models is increased from 4 to 8 to 16 radicals, convergence is observed to susceptibility values slightly above the experimental ones, "over-shooting" slightly. The "over-shooting" is mitigated by the inclusion of the HB-PYR molecules which improve the calculation of the magnetic susceptibility curves.

Section 6 - Spin Densities and SOMO's for Dimer Magnetic Models

For **CuXMI**, the relatively large magnitude and the sign of J_1, the intra-dimer exchange coupling, can be attributed to the significant orthogonal overlap of the SOMO orbitals in the dimer (see Fig. S6.1(a) and (b) for α- and β-SOMO of the open-shell singlet state, respectively). This leads to a strong FM Cu-X-Cu (X = Cl^-, Br^-) through-bond interaction within the dimer, in agreement with the Goodenough-Kannamori rules.[14,15] The spin density of the dimer shows that the unpaired electron is delocalised over the Cu atom, X atom, and O atom on the MI ligand.

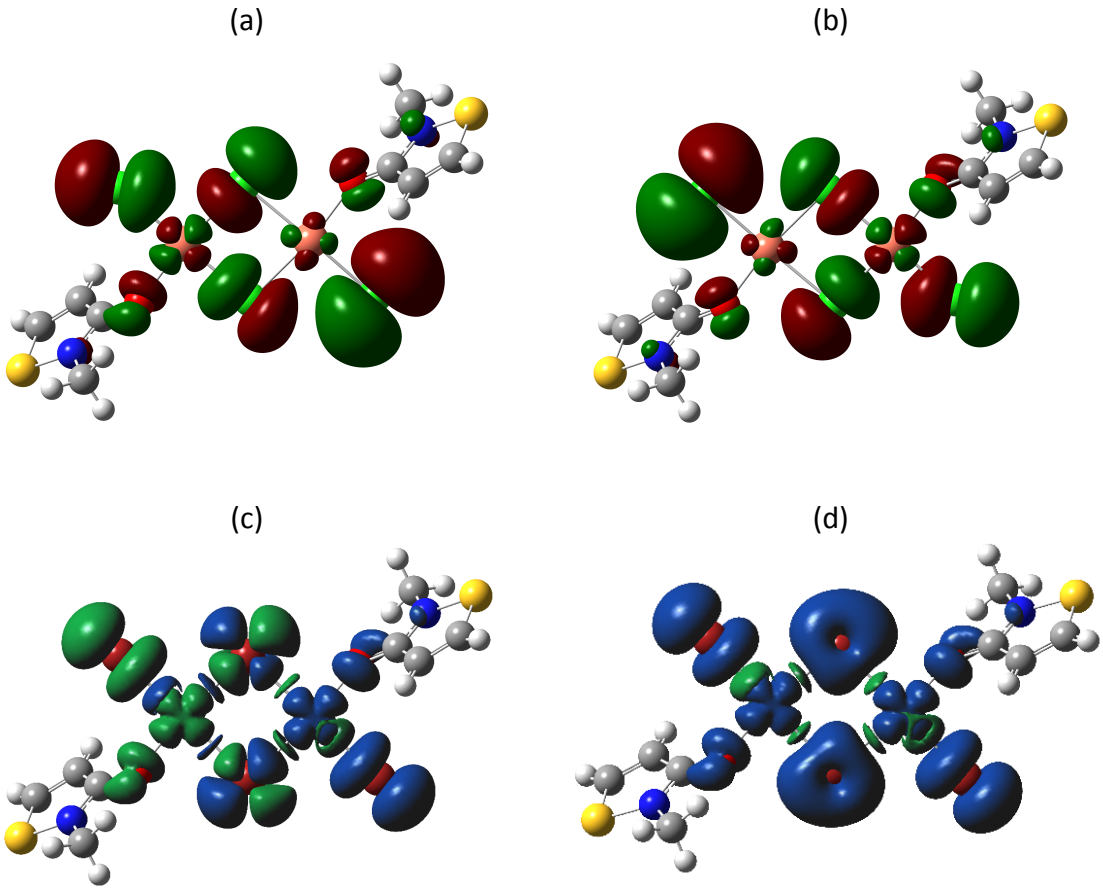

Figure S6.1. Singly occupied molecular orbital (a) α- and (b) β-(SOMO) of the open-shell singlet of the d_1 dimer pair in **CuClMI**. The spin density of the d_1 dimer model for **CuBrMI** for (c) the open-shell singlet, and (d) triplet states. The SOMO and spin density plots are plotted at an isovalue of 0.02 and 0.004, respectively. Colour code in c-d): green and blue indicates negative and positive spin densities, respectively.

Section 7 – Calculation of the Magnetic Properties of CuClMI

In the calculation of the individual magnetic exchange interactions using the FPBU method[3], the AFM interaction J_3 in **CuClMI** appeared to be incorrect, since from the experimental data reported in the literature,[2] the overall magnetic interaction in **CuClMI** should be FM between dimers. However, as indicated in the manuscript, the FPBU method predicted an AFM J_3 interaction. Prior to re-collecting the experimental magnetic data for **CuClMI**, which proved that the experimental data previously reported[2] is questionable, extensive testing was done to identify possible problems occurring in the FPBU method. All the information extracted after considering various aspects is discussed below, including the effect of optimizing the geometry of the organic ligand, the effect of the halide ligands, the effect of the magnetic field and the effect of temperature.

Effect of structure optimization

There is a small difference in the geometries of the organic ligands of the experimental structures **CuClMI** and **CuBrMI**. To investigate whether the structural differences were the origin of the different magnetic exchange, magnetic exchange interactions in **CuClMI** were probed by optimizing the positions of atoms in the MI ligand and fixing the positions of specific atoms to maintain the main structural features and geometry in Gaussian[4]. The positions of the Cu(II) ions, chloride ligands, and O1, C1 and C2 atoms (see Fig. 2 in the main text for numbering) were fixed in each dimer pair d_1-d_4 to retain the orientation of the dimer pair (see Fig. S2.1), while the positions of the S1, N1, C3, C4 atoms and all hydrogen atoms were optimized. The most significant difference between the optimized *vs.* experimental structures was longer C-H bond lengths. As shown in Table S7.1 there is not a significant difference in the exchange interaction values J_1-J_4 upon optimizing the **CuClMI** structure, but interestingly the most affected interaction is J_3 coupling, which is the interaction that determines whether the compound exhibits FM or AFM interactions at low temperatures. Small structural changes in the optimized **CuClMI** structure create a 10% decrease in the magnitude of J_3. This suggests that J_3 interaction is highly sensitive to structural changes, which makes it a good candidate to tune the bulk magnetic properties of these materials.

Table S7.1. Comparison of interactions J_1-J_4 calculated for **CuClMI** to assess the effect of optimisation of the organic ligand geometry on the magnetic exchange values. J_i values are given in cm^{-1}.

	Gaussian09(D)	
	CIF	**Optimized**
J_1	28.16	28.10
J_2	0.61	0.56
J_3	-5.55	-5.09
J_4	1.12	1.13

Effect of exchange of halides on J_1-J_4

To test whether an exchange of chloride ligands with bromide ligands in structure **CuClMI** (and *vice versa*) can reverse the bulk magnetic response, the calculation of interactions J_1-J_4 was repeated by changing the type of halide ions (in the Gaussian[4] input files). The results are shown in Table S7.2. The name **CuXMI** refers to the original structure whereas **Cu(X)MI** refers to the substituted structure. The exchange of the bromide ligands in structure **CuBrMI** with chloride ligands (comparison of **CuBrMI** and **Cu(Cl)MI**) results in smaller *J* values for all pairs. This is in agreement with the current understanding. Substitution of the chloride ligands in **CuClMI** with bromide ligands allows for the comparison of **CuClMI** and **Cu(Br)MI**. This substitution results in significantly larger magnetic exchange interactions. Therefore, the exchange interaction between dimers only differ in magnitude, and no reversal of properties occurs, upon change of the identity of the halide ion, which does not explain why FM properties have been reported for the chloride analogue.[2]

Table S7.2. Effect of exchange of halide ligands in structures **CuClMI** and **CuBrMI**. **Cu(Cl)MI** and **Cu(Br)MI** refer to the substituted structures where the halide ions have been exchanged. J_i values are given in cm^{-1}.

	CuBrMI	**Cu(Cl)MI**	**CuClMI**	**Cu(Br)MI**
J_1	**42.10**	24.97	**28.16**	53.69
J_2	**1.15**	0.45	**0.61**	1.80
J_3	**-9.81**	-3.10	**-5.55**	-19.75
J_4	**2.26**	1.17	**1.12**	2.18

Effect of the magnetic field

To test the effect that the external magnetic field has on the simulated susceptibility data, the energy levels of both the 2x8 and 2x8 cyclic models were calculated while varying the external magnetic *B*-field (see Fig. S7.1 for results). As the magnetic field is increased, a higher response is observed at low temperatures, reaching a maximum around 5 T and then the response decreased at a field strength > 5 T. There appears to be little difference in the response generated by the open and cyclic models. Although a FM response can be elicited from the 2x8 models, the field required to do so was far above the 1 T field used in the literature[2] and can also be discarded as a source of FM interactions in **CuXMI** derivatives.

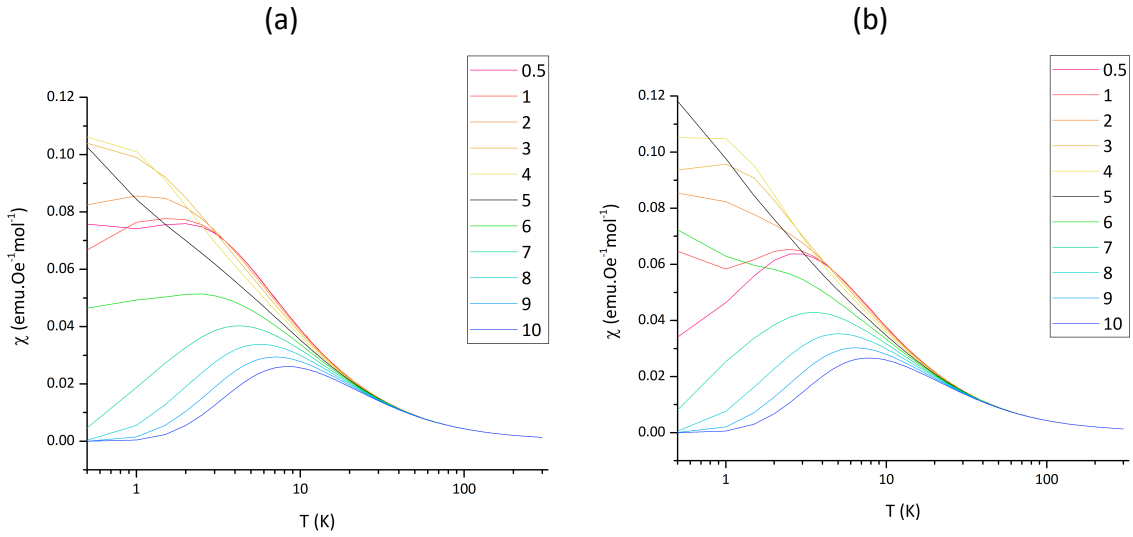

Figure S7.1. External (B-field) dependence on the simulated susceptibility data of the (a) 2x8 open model and (b) 2x8 cyclic model using J_{iT}.

Contraction of Polymer

In the absence of a low-temperature structure (sub 10 K) for **CuClMI**, the contraction of the structure along the polymer axis, which is expected to occur on reduction of the temperature, was mimicked by reducing the inter-dimer spacing of dimer pair d_3 incrementally by 10 %. A linear decrease of J_3 is observed, with values listed in Table S7.3, indicating that lowering of the temperature increases the AFM interaction between the dimers. The effect of J_2 and J_4 were not considered due to the small values of these interactions.

Table S7.3. Dependence of interaction J_3 on inter-dimer spacing.

Inter-dimer spacing (Å)	J_3 (cm^{-1})
3.04149	-10.18
3.01108	-11.97
2.98066	-12.89
2.95025	-13.88
2.91983	-14.93
2.88942	-16.05
2.85900	-17.24
2.82859	-18.51
2.79817	-19.86
2.76776	-21.29
2.73734	-22.81

Dependence of bulk magnetic properties of CuClMI on inter-dimer interaction J_3

To understand under which conditions **CuClMI** can behave as a ferromagnet the interactions between dimers were probed by varying the largest inter-dimer exchange interaction, J_3, systematically from J_3 to -J_3 with the results illustrated in Fig. S7.2. A reversal of properties to FM is observed at J_3 = 0 cm^{-1} since the magnetic topology then becomes that of isolated FM dimers. As the J_3 interaction is increased (more FM), the response becomes more FM, and the experimental reported data[2] can be reproduced quite well with J_3 = +2.83 cm^{-1}, which would correspond to a FM spin-ladder topology.

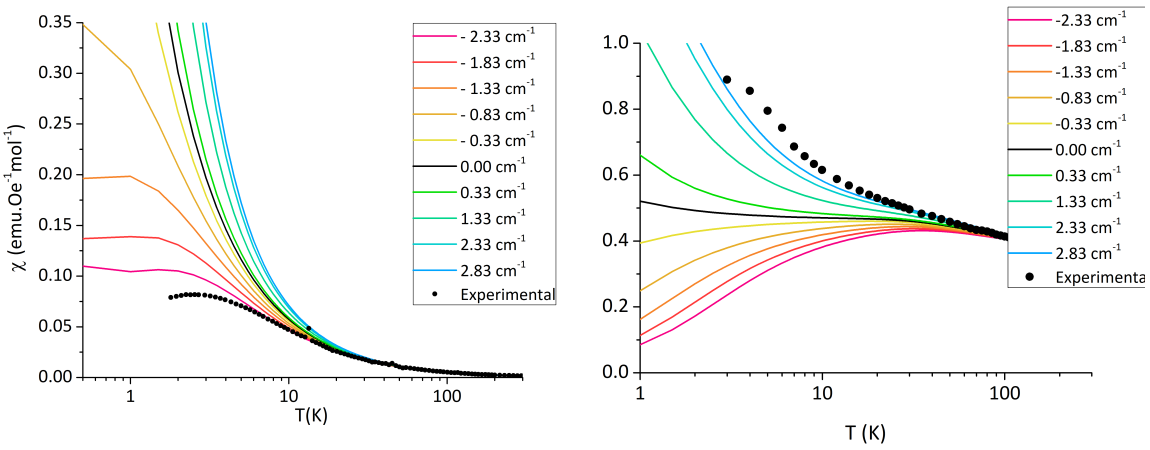

Figure S7.2. Simulated (a) $\chi_m(T)$ and (b) $\chi_m T(T)$ curves' dependence on exchange interaction J_3. Reversal of AFM to FM occurs at J_3 = 0 (black line). "Experimental" refers to the experimental data recorded in (a) this study and (b) Kato *et al.*[2]

In summary, **CuClMI** can become a ferromagnet by fine-tuning the inter-dimer d_3 interaction. However, this cannot be attained with chloride or any other halide ligand as bridging ligand between Cu(II) ions, suggesting that the only conditions in which a FM value for J_3 can be obtained is *via* the organic ligand. This is also confirmed by the results obtained for structure **CuClMI(Rot)** as reported in the main text.

Section 8 – Comparison of magnetic data for CuClMI

In an attempt to eliminate the noise observed in the experimental magnetic data recorded for **CuClMI** in this study (blue circles in Fig. S8.1), a second data set was collected using another sample (37.7 mg) from the same batch of **CuClMI** (red triangles in Fig. S8.1). In the new data set, the anomalies observed above 30 K exhibit a random pattern. It was later determined that power surges occurred in the building causing these erratic data. The anomaly at 15 K is observed in both samples, indicating that it is systematically present. The shape of the anomaly at 15 K is different in the two data sets but occur at the same temperature. This anomaly may indicate a phase transition occurring at 15 K, but this cannot be said with certainty, and specialised experiments would be required to confirm this. This falls outside the scope of the current study.

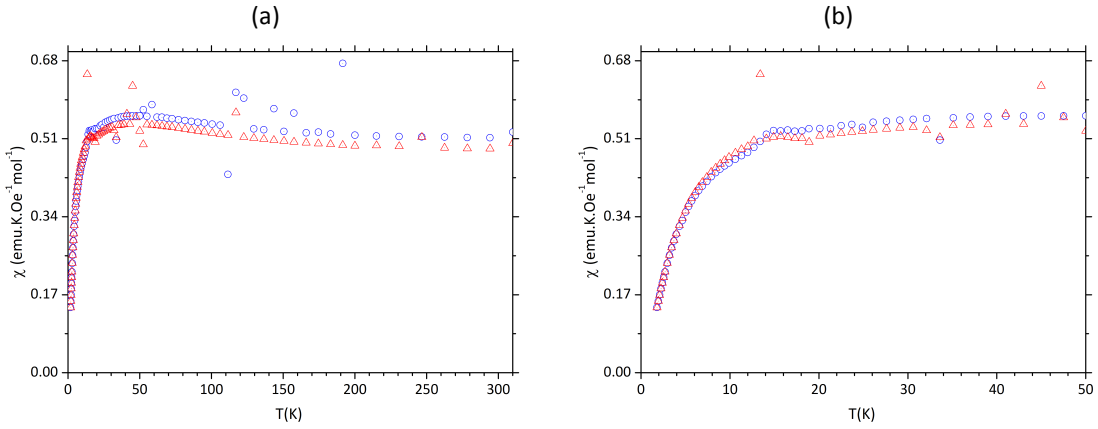

Figure S8.1. (a) Experimental $\chi_m T$ product data reported in the main text (blue circles) and the second data set measured on a different sample (red triangles) of **CuClMI**. Note the random pattern of the signal noise > 30 K and (b) the anomaly evident at ~15 K.

Section 9 – Energy spectra and thermal population

For **CuBrMI** the interaction between the triplet dimers is AFM for J_3. In addition, two very weak competing NNN FM interactions are calculated for J_2 and J_4. At T > 10 K there are thousands of occupied spin states and the material essentially behaves as a paramagnet as seen from the results of a Boltzmann population analysis of the simulated energies, listed in Table S9.1. As the temperature decreases, these states become depopulated. At T_{max} = 6.5 K and 3 K, the temperature at which the maxima in the simulated χ_m data for **CuBrMI** and **CuClMI** respectively occurs, the 2x8 cyclic model using J_{iT}, indicates that many low spin configurations are still populated with a low average total spin, $\bar{S} \approx 1.4$. However, as the temperature decreases below T_{max} , most of these states become depopulated too, and the lower singlet E_0 and triplet E_1 states become more populated (see Table S9.1), which results in a decrease in the overall susceptibility, until a temperature of 0.5 K is reached, where the singlet E_0 state is the only significantly occupied state for both compounds. The magnetic ground state for both compounds is, therefore, a singlet state, most likely due to the triplet dimers interacting with opposing spins along the ladder. In contrast, **CuClPYR** has hight spin states at low temperatures, leading to FM bulk properties.

Table S9.1. Boltzmann population analysis of simulated energies of **CuXMI** and **CuClPYR**. E_i refers to eigenvalue energies obtained from solving the Heisenberg Hamiltonian equation, and S refers to the total spin of the corresponding state.

	CuClMI				**CuBrMI**				**CuClPYR**			
		Occupation (%)				**Occupation (%)**				**Occupation (%)**		
E_i	**S**	**0.5 K**	**3 K**	**6.5 K**	**S**	**0.5 K**	**3 K**	**6.5 K**	**S**	**0.5 K**	**5 K**	**10K**
E_0	0	96	16	< 0.1	0	100	59	13	8	34	0.7	0.3
E_1	1	4	10	< 0.1	1	< 0.1	19	7	7	21	0.6	0.3
E_2	2	< 0.1	4	< 0.1	1	< 0.1	3	3	6	12	0.6	0.3
E_3	1	< 0.1	3	< 0.1	1	< 0.1	3	3	5	7	0.6	0.3
E_4	1	< 0.1	3	< 0.1	2	< 0.1	3	3	7	5	0.6	0.3
E_5	0	< 0.1	3	< 0.1	1	< 0.1	2	2	4	4	0.5	0.2
E_6	2	< 0.1	3	< 0.1	1	< 0.1	2	2	6	3	0.5	0.2
E_7	1	< 0.1	2	< 0.1	0	< 0.1	1	2	3	2	0.5	0.2
E_8	1	< 0.1	2	< 0.1	1	< 0.1	1	2	5	2	0.5	0.2
E_9	0	< 0.1	2	< 0.1	1	< 0.1	1	2	4	1	0.5	0.2
$\sum_1^{100} E_i$†	1.49‡	4	20	41	1.42‡	< 0.1	40	68	3.78‡	66	32	19

† This refers to the sum of E_1 to E_{100}, excluding E_0

‡ This refers to $\bar{S}$

The temperature-dependent Boltzmann populations of the calculated energy states of the cyclic 2x8 models using J_{iT} for **CuClMI** and **CuBrMI** are illustrated in Fig. S9.1.

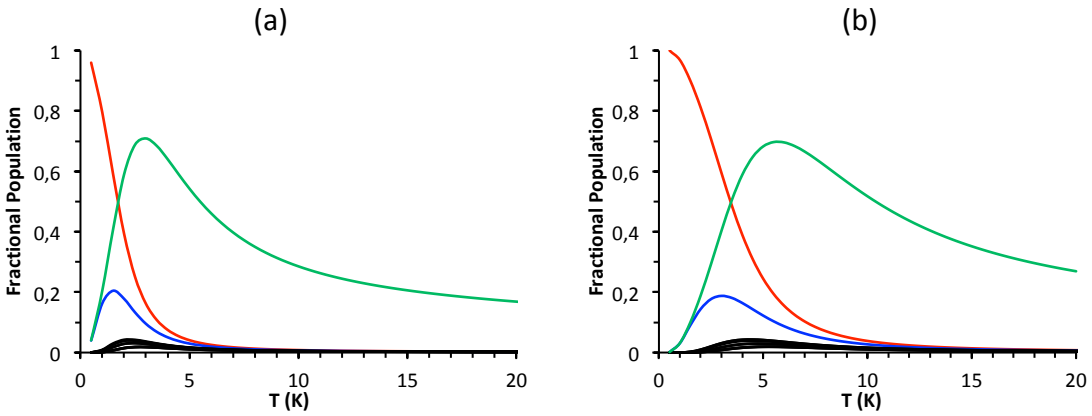

Figure S9.1. Temperature-dependent Boltzmann population of low-lying energy states of (a) **CuClMI** and (b) **CuBrMI** using the cyclic 2x8 models and J_{iT}. The population of the E_0 singlet state (red) E_1 triplet state (blue) and the other low-lying states' populations (black). The sum of the populations of the 100 lowest states is given in green.

References

1 Vreshch, V. DiffractWD: an open-source program for powder pattern comparison and visualization, *J. Appl. Crystallogr.* 2010, **44**, 219–220.

2 M. Kato, K. Hida, T. Fujihara, and A. Nagasawa, Ferromagnetic Spin Ladder System: Stack of Chlorido-Bridged Dinuclear Copper({II}) Complexes with 2-Methylisothiazol-3(2H)-one, *Eur. J. Inorg. Chem.* 2010, **2011**, 495–502.

3 J.J. Novoa, M. Deumal, and J. Jornet-Somoza, Calculation of microscopic exchange interactions and modelling of macroscopic magnetic properties in molecule-based magnets, *Chem. Soc. Rev.* 2011, **40**, 3182.

4 M.J. Frisch, G.W. Trucks, H.B. Schlegel, G.E. Scuseria, M.A. Robb, J.R. Cheeseman, G. Scalmani, V. Barone, B. Mennucci, G.A. Petersson, H. Nakatsuji, M. Caricato, X. Li, H.P. Hratchian, A.F. Izmaylov, J. Bloino, G. Zheng, J.L. Sonnenberg, M. Hada, M. Ehara, K. Toyota, R. Fukuda, J. Hasegawa, M. Ishida, T. Nakajima, Y. Honda, O. Kitao, H. Nakai, T. Vreven, J.A. Jr. Montgomery, J.E. Peralta, F. Ogliaro, M.J. Bearpark, J.J. Heyd, E. Brothers, K.N. Kudin, V.N. Staroverov, R. Kobayashi, J. Normand, K. Raghavachari, A. Rendell, J.C. Burant, S.S. Iyengar, J. Tomasi, M. Cossi, N. Rega, J.M. Millam, M. Klene, J.E. Knox, J.B. Cross, V. Bakken, C. Adamo, J. Jaramillo, R. Gomperts, R.E. Stratmann, O. Yazyev, A.J. Austin, R. Cammi, C. Pomelli, J.W. Ochterski, R.L. Martin, K. Morokuma, V.G. Zakrzewski, G.A. Worth, P. Salvador, J.J. Dannenberg, S. Dapprich, A.D. Daniels, Ö. Farkas, J.B. Foresman, J.V. Ortiz, J. Cioslowski, and D.J. Fox, Gaussian 09 Revision D.01, 2009.

5 F. Neese, Wiley Interdiscip. Rev.: Comput. Mol. Sci., 2018, 8, e1327.

6 B.H. Brandow, Linked-Cluster Expansions for the Nuclear Many-Body Problem, *Rev. Mod. Phys.* 1967, **39**, 771-828.

7 P. Durand, and J.-P. Malrieu, *Advances in Chemical Physics,* John Wiley & Sons, Inc., Hoboken, 1987.

8 O. Kahn, *Molecular Magnetism*, VCH, 1993.

9 T. Terencio, R. Bastardis, N. Suaud, D. Maynau, J. Bonvoisin, J.-P. Malrieu, C.J. Calzado, and N. Guihéry, Physical analysis of the through-ligand long-distance magnetic coupling: spin-polarization versus Anderson mechanism, *Phys. Chem. Chem. Phys.* 2011, **13**, 12314-12320.

10 G. David, F. Wennmohs, F. Neese, and N. Ferré, Chemical Tuning of Magnetic Exchange Couplings Using Broken-Symmetry Density Functional Theory, *Inorg. Chem.* 2018, **57**, 12769-12776.

11 P.W. Anderson, Antiferromagnetism. Theory of Superexchange Interaction, *Phys. Rev.* 1950, **79**, 350-356

12 E. Coulanud, N. Guihéry, J.-P. Malrieu, D. Hagebaum-Reignier, D. Siri, and N. Ferré, Analysis of the physical contributions to magnetic couplings in broken symmetry density functional theory approach, *J. Chem. Phys.* 2012, **137**, 114106

13 K.C. Shortsleeves, M.M. Turnbull, C.B. Seith, E.N. Tripodakis, F. Xiao, C.P. Landee, L.N. Dawe, D. Garrett, G.D. de Delgado and B.M. Foxman, Crystallographic and magnetic studies of the 2-pyridone/copper halide system, *Polyhedron*, 2013, **64**, 110–121.

14 J.B. Goodenough, Theory of the Role of Covalence in the Perovskite-Type Manganites [La, M({II})]{MnO}$_3$, *Phys. Rev.* 1955, **100**, 564–573

15 J. Kanamori, Superexchange Interaction and Symmetry Properties of Electron Orbitals, *J. Phys. Chem. Solids* 1959, **10**, 87–98.